Voltage Oriented Control Design for Brushless Doubly-Fed Reluctance Machines

Taufik Taluo, Leposava Ristić, *Member, IEEE* and Milutin Jovanović, *Senior Member, IEEE*

***Abstract*— The paper considers voltage vector oriented control (VOC) of a promising brushless doubly-fed reluctance machine (BDFRM) for large-scale wind turbines or pump drives. The BDFRM has been receiving increasing attention due to its low operation and maintenance costs achieved by using partially-rated power electronics and a highly reliable brushless construction. Furthermore, the BDFRM may provide competitive performance to its traditional slip-ring counterpart, the doubly-fed induction machine (DFIM). The BDFRM has been modeled in MATLAB/Simulink with the VOC being implemented to both the machine and grid side converter bridge to provide a bi-directional power flow. Aspects concerning proportional integral (PI) controllers optimal tuning have been considered and comprehensive simulation results presented to demonstrate the obtained VOC response under the unity power factor and maximum torque per inverter ampere conditions.**

Index Terms*— *brushless doubly-fed reluctance machine, Voltage Vector oriented control, dynamic modeling, power electronics, wind generators.

I. Introduction

Brushless doubly-fed reluctance machines (BDFRMs) have become increasingly popular as an attractive alternative solution to the compromised reliability and high maintenance requirements associated with the brush gear of conventional doubly fed induction machines (DFIMs) [1]. At the same time, they retain similar cost advantages due to the reduced power electronics rating in centrifugal pump drives (typically 25-30% of the fully rated converters) and wind energy conversion systems with 2:1 speed ranges [2]. The BDFRM shares all the advantages of doubly-fed machines compared to singly-fed counterparts, such as, the operational mode flexibility, the greater control freedom, and the possibility of sub-synchronous and super-synchronous speed mode in either motoring or generating regime. It can operate as an induction machine (which is an important "fail-safe" measure in case of the inverter failure) or as a classical wound rotor synchronous turbo-machine [3-4]. Besides, the BDFRM is inherently medium-speed in nature, and it allows the use of a more compact 2-stage gearbox for wind turbines unlike the failures prone 3-stage counterpart of the high-speed DFIM commonly deployed in these applications. Generally, the BDFRM has a larger leakage reactance than an equivalent DFIM due to the modest coupling between the windings. Owing to this and the consequently lower fault current levels, the low-voltage-fault-ride-through (LVFRT) of the BDFRG may be accomplished safely without a crowbar protection circuitry [5-7].

Taufik Taluo and Leposava Ristić are with the School of Electrical Engineering, University of Belgrade, 73 Bulevar kralja Aleksandra, 11020 Belgrade, Serbia (e-mail: leposava.ristic@etf.bg.ac.rs).

Milutin Jovanović is with the Northumbria University at Newcastle, UK (e-mail: milutin.jovanovic@northumbria.ac.uk).

Various control approaches have been addressed in the BDFRM literature over the years including scalar control [2], [8-10], vector or field-oriented control (VC/FOC) [2], [6], [9], [11], [12], direct torque control [13-16], and direct power control [17]. A comparative analysis of these control methods has been presented in [13]. In [18] a predictive direct power control (PDPC) method has been proposed to overcome the variable switching frequency resulting from the use of hysteresis current controllers.

In this paper, the VOC of the BDFRM has been modeled and simulated in both motoring and generating operating modes for two different control objectives namely, the unity power-factor of the machine primary (grid side converter) and the maximum torque per inverter ampere (MTPIA) strategy. Such a comparative case study for a custom-designed 2 MW BDFRM has been selected to illustrate a potential efficiency improvement, which can be gained by reducing both the secondary winding copper and inverter switching losses.

The paper is organized as follows: after the Introduction, the second section deals with dynamic model of BDFRM. Section III describes control strategy of the machine side converter with emphasis on the design methodology for the applied PI controllers, while Section IV separately describes the design methodology for the speed PI controller. Vector control of the grid side converter is presented in Section V. Results of simulations for both motoring and generating operation are presented in Section VI. The conclusion is given in Section VII.

II. Dynamic Model

Unlike conventional machines, the BDFRM has two standard, sinusoidally distributed stator windings of different applied frequencies and pole numbers (Fig. 1), the grid-connected primary (power) winding, and the inverter-fed secondary (control) winding. The indirect magnetic coupling between the windings, a pre-requisite for the machine torque production, is achieved through a suitably designed modern cage-less reluctance rotor structure with half the total number of the stator poles.

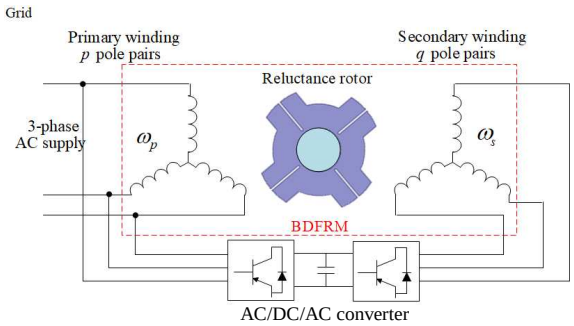

Fig. 1. A conceptual diagram of the BDFRM

The space-vector voltage and flux equations for the BDFRM in a stationary reference frame using standard notation and assuming motoring convention are [19]:

$$\left.\begin{aligned}\underline{v}_{p_s} &= R_p\underline{i}_{p_s} + \frac{d\underline{\lambda}_{p_s}}{dt} = R_p\underline{i}_{p_s} + \left.\frac{d\underline{\lambda}_{p_s}}{dt}\right|_{\theta_p \text{ const}} + j\omega_p\underline{\lambda}_{p_s} \\ \underline{v}_{s_s} &= R_s\underline{i}_{s_s} + \frac{d\underline{\lambda}_{s_s}}{dt} = R_s\underline{i}_{s_s} + \left.\frac{d\underline{\lambda}_{s_s}}{dt}\right|_{\theta_s \text{ const}} + j\omega_s\underline{\lambda}_{s_s}\end{aligned}\right\} \quad (1)$$

$$\left.\begin{aligned}\underline{\lambda}_{p_s} &= L_p\underline{i}_{p_s} + L_{ps}\underline{i}^*_{s_s}e^{\theta_r} \\ \underline{\lambda}_{s_s} &= L_p\underline{i}_{s_s} + L_{ps}\underline{i}^*_{p_s}e^{\theta_r}\end{aligned}\right\} \quad (2)$$

If we choose for the primary winding a rotating frame aligned with the primary flux linkage vector rotating at ω_p, and for the secondary quantities a frame rotating at $(\omega_r - \omega_p)$, then (1) and (2) can be rewritten as follows:

$$\left.\begin{aligned}\underline{v}_p &= R_p\underline{i}_p + \frac{d\underline{\lambda}_p}{dt} + j\omega_p\underline{\lambda}_p \\ \underline{v}_s &= R_s\underline{i}_s + \frac{d\underline{\lambda}_s}{dt} + j(\omega_r - \omega_p)\underline{\lambda}_s\end{aligned}\right\} \quad (3)$$

$$\left.\begin{aligned}\underline{\lambda}_p &= L_p\underline{i}_p + L_{ps}\underline{i}^*_{s_m} \\ \underline{\lambda}_s &= L_p\underline{i}_s + L_{ps}\underline{i}^*_{p_m} = \sigma L_s\underline{i}_s + \underbrace{\frac{L_{ps}}{L_p}\underline{\lambda}^*_p}_{\underline{\lambda}_{ps}}\end{aligned}\right\} \quad (4)$$

where σ = 1- L^2_{ps} / (L_pL_s) is the leakage factor, and λ_{ps} is the primary flux linking the secondary winding (i.e. the mutual flux linkage). The fundamental angular velocity and torque relationships for the machine with p_r=p+q rotor poles and $\omega_{p,s} = 2\pi f_{p,s}$ applied frequencies to the respective 2p-pole primary and 2q-pole secondary windings are [19]:

$$\omega_{rm} = \frac{\omega_p + \omega_s}{p_r} \Leftrightarrow n_{rm} = 60\frac{f_p + f_s}{p_r} \quad (5)$$

$$T_e = \frac{3p_rL_{ps}}{2L_p}(\lambda_{pd}i_{sq} + \lambda_{pq}i_{sd}) = \frac{3p_r}{2}(\lambda_{ps_d}i_{sq} - \lambda_{ps_q}i_{sd}) \quad (6)$$

It is worth mentioning that while all the ω_p rotating vectors in the primary voltage and flux equations are in ω_p reference frame, the secondary counterparts, including the λ_{ps} components, are rotating at ω_s and are in $p_r\omega_{rm} - \omega_p = \omega_s$ reference frame (Fig. 2). Note also that the secondary and primary magnetizing currents, i_{sm} and i_{pm}, rotate at ω_p and ω_s respectively, contrary to their source vectors, i_s and i_p, having the same magnitudes and relative angular positions in the complementary reference frames (i.e. $i_{sm} = i_s$ and $i_{pm} = i_p$) and rotating at different velocities, ω_s and ω_p, as shown in Fig. 2. This peculiar frequency modulation process comes from the reluctance rotor action in the process of electro-mechanical energy conversion [11], [19]. The mechanical power equation showing individual contributions of each winding is:

$$P_m = T_e\omega_{rm} = \underbrace{\frac{T_e\omega_p}{p_r}}_{P_p} + \underbrace{\frac{T_e\omega_s}{p_r}}_{P_s} = P_p\left(1 + \frac{\omega_s}{\omega_p}\right) \quad (7)$$

The machine operating mode is determined by the power flow through the primary side i.e. from the grid for the motor (T_e > 0), and to the grid for the generator (T_e < 0), while the secondary can consume or deliver real power subject to the winding phase sequence, i.e. the ω_s sign: the BDFRM would absorb (produce) positive secondary power at super (sub)-synchronous speeds as a motor, and at sub (super)-synchronous speeds as a generator. Voltage oriented control (VOC) scheme has been implemented for both the machine side converter (MSC) and the grid side converter (GSC). This allows a bi-directional power flow through the secondary winding for either motoring or generating operation. Both VOC controllers have inner (current control) and external (power control) loops.

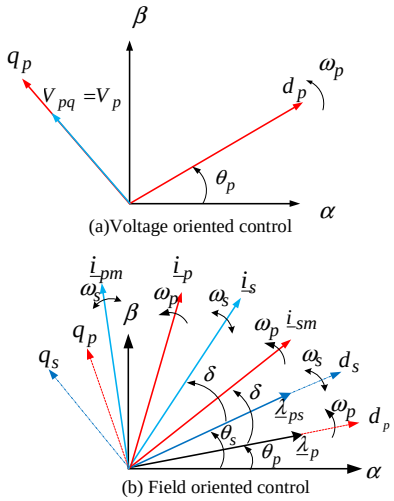

Fig. 2. Reference frames and space vectors.

The VOC of the MSC requires measurements of the primary and secondary *d*-*q* currents, the primary voltage and the rotor position, a suitable Park transformation unit and *PI* current controllers to adjust the reference *d*-*q* voltages as the output values from the control unit.

III. Machine Side Vector Control (MSVC)

The MSVC scheme is shown in Fig. 3. The external loop has two *PI* controllers to regulate the primary reactive and active power independently, so does the inner one but to control the *d*-axis and *q*-axis secondary currents.

A. *Inner (current) control loops*

According to the BDFRM steady-state model, the secondary *d*-*q* voltages can be identified as:

$$\left.\begin{aligned}v_{sd} &= R_si_{sd} + \omega_s(\sigma L_si_{sd} + \lambda_{ps_d}) \\ v_{sq} &= R_si_{sq} + \omega_s(\sigma L_si_{sq} + \lambda_{ps_q})\end{aligned}\right\} \quad (8)$$

The above equation is important for the vector control algorithm and has been used to calculate the reference voltage values. Due to the fairly constant flux linkage offset component, the use of *PI* current controllers is justified for this purpose and can be formulated by [11]:

$$\left.\begin{aligned}v^*_{sd} &= PI(i^*_{sd} - i_{sd}) \\ v^*_{sq} &= PI(i^*_{sq} - i_{sq})\end{aligned}\right\} \quad (9)$$

The current control loop on its own is shown in Fig. 4. The corresponding transfer function can be written as follows:

$$\frac{i_{dq_s}(s)}{i^*_{dq_s}(s)} = \frac{\frac{k_P}{\sigma L_s}s + \frac{k_I}{\sigma L_s}}{s^2 + \frac{R_s + k_P}{\sigma L_s}s + \frac{k_I}{\sigma L_s}} \quad (10)$$

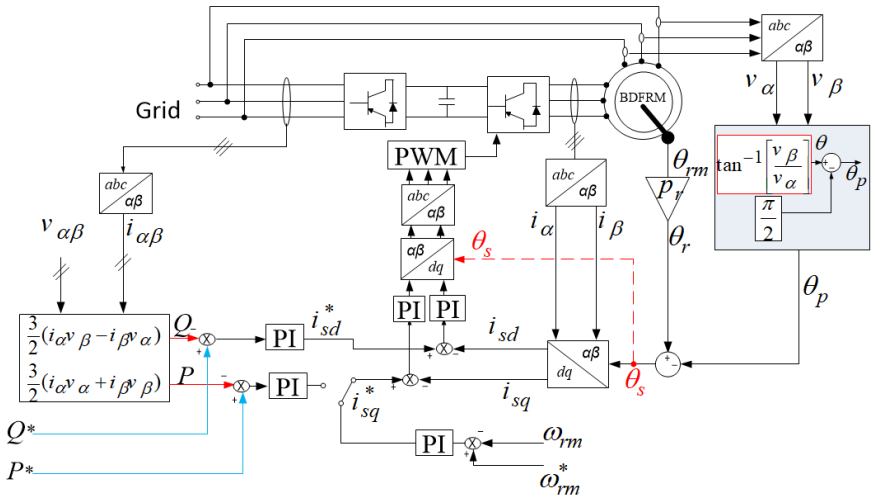

Fig. 3. Block diagram for the machine side converter control.

Assuming $k_P << k_I$ [20], (10) can be approximated as a second-order transfer function of the following form:

$$\frac{i_{dq_s}(s)}{i^*_{dq_s}(s)} = \frac{\frac{k_I}{\sigma L_s}}{s^2 + \frac{R_s + k_P}{\sigma L_s}s + \frac{k_I}{\sigma L_s}} = \frac{\omega_n^2}{s^2 + 2\xi\omega_n s + \omega_n^2} \tag{11}$$

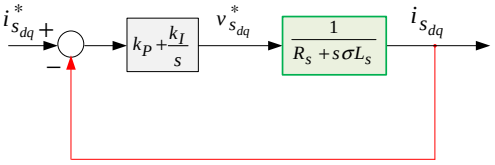

Fig. 4. Current control loop of the secondary-side converter.

Here ξ (11) is defined as the damping ratio. It influences the maximum overshoot and response speed. In a classical second-order system design, an optimum damping ratio is considered as 0.707, which gives a very small overshoot (less than 5%) with a reasonable settling time. The undamped natural frequency ω_n affects the response speed. The PI current controller gains are given as:

$$k_P = (2\xi\omega_n\sigma L_s - R_s), \qquad k_I = \omega_n^2\sigma L_s \tag{12}$$

B. Power Loop Derivation

The power control relationships can be derived from the dynamic model voltage equations (3), where the respective vector components appear as DC in steady state. Substituting $\underline{i}_p$ from the $\underline{\lambda}_p$ equation in (2) into expression $S_p = (3/2)\underline{v}_p\underline{i}_p^*$, one can develop the following important VOC relations for the active and reactive power [6], [11]:

$$\left.\begin{aligned} P_{p(\mathrm{VOC})} &= \frac{3\omega_p}{2}(\lambda_{ps_d} i_{sq} - \lambda_{ps_q} i_{sd}) = P_{p(\mathrm{FOC})} \frac{3\omega_p}{2}\lambda_{ps_q} i_{sd} \\ Q_{p(\mathrm{VOC})} &= \frac{3\omega_p}{2}\left(\frac{\lambda_p^2}{L_p} - \lambda_{ps_d} i_{sd} - \lambda_{ps_q} i_{sq}\right) = Q_{p(\mathrm{FOC})} \frac{3\omega_p}{2}\lambda_{ps_q} i_{sq} \end{aligned}\right\} \tag{13}$$

In VOC, P_p and Q_p are coupled as both the i_{sd} and i_{sq} secondary currents appear in (13). The level of coupling can be reduced by aligning the q_p-axis of the reference frame to the primary voltage vector as presented in Fig. 2(a). In this case, λ_p would be phase shifted ahead of the corresponding d_p-axis, depending on the winding resistance, which is generally smaller as the machine is larger. Therefore, for the frame alignment choice presented in Fig. 2, VOC could be similar to FOC as $\lambda_{ps_d} \gg \lambda_{ps_q}$, i.e. $\lambda_{ps_d} \approx \lambda_{ps}$ and the equation (13) becomes:

$$\left.\begin{aligned} P_{p(\mathrm{VOC})} &\approx P_{p(\mathrm{FOC})} = \frac{3\omega_p}{2}\lambda_{ps} i_{sq} \\ Q_{p(\mathrm{VOC})} &\approx Q_{p(\mathrm{FOC})} = \frac{3\omega_p}{2}\left(\frac{\lambda_p^2}{L_p} - \lambda_{ps} i_{sd}\right) = \frac{3\omega_p}{2}\lambda_p i_{pd} \end{aligned}\right\} \tag{14}$$

With the λ_p and λ_{ps} magnitudes being fixed by the primary winding grid connection at line frequency (ω_p), P_p and Q_p are proportional to i_{sq} and i_{sd} currents respectively according to (14), which means that the use of PI controllers is valid [11]:

$$\left.\begin{aligned} i^*_{sd} &= PI(Q^*_P - Q_P) \\ i^*_{sq} &= PI(P^*_P - P_P) \end{aligned}\right\} \tag{15}$$

Since the current control loops are much faster than the power control loops, the converter dynamics and measurement delays can be neglected [20], [21], as shown in Fig. 5.

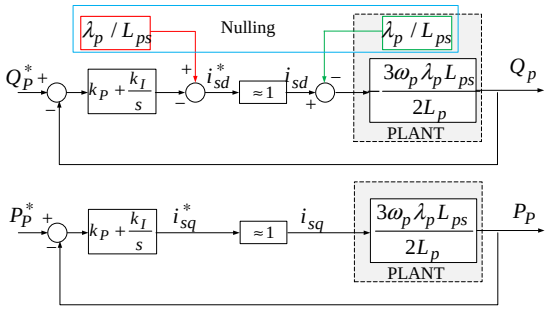

Fig. 5. Power control loops of the secondary-side converter.

Transfer functions for the active and reactive power are the same and can be expressed as:

$$\frac{Q^*_p}{Q_p} = \frac{P^*_p}{P_p} = \frac{As+1}{\left(\frac{1}{Bk_I} + A\right)s + 1} \tag{16}$$

where $A = k_P / k_I$, $B = (3/2)V_p\left(L_{ps} / L_p\right)$.

If A is the dominant term in the denominator (i.e. $A \approx A+1/(Bk_I)$), then the transfer function is close to a unity gain with a poor noise rejection property. Thus, A should be very small in order to use a first order approximation of the transfer function and to determine the PI gains as follows:

$$TF_o = \frac{P_p^*}{P_p} = \frac{Q_p^*}{Q_p} = \frac{As+1}{(\frac{1}{Bk_I}+A)s+1} \approx \frac{1}{\tau_o s+1} \quad (17)$$

$$k_I = \frac{1}{B(\tau_o - A)} \quad , \quad k_P = Ak_I \quad (18)$$

IV. Speed Loop in Vector Control

Vector control is appropriate for most drive and generator applications due to the high quality response provided at fixed sampling rates. The inner loop is to control the current components (one for each reference frame axis), while the external one corresponds to the speed control. Through the speed controller action, the appropriate torque is developed as presented in Fig. 6. In this case (i.e. VOC), the torque expression is simplified as:

$$T_e = \frac{3p_r L_{ps}}{2L_p}\lambda_p i_{sq} \quad (19)$$

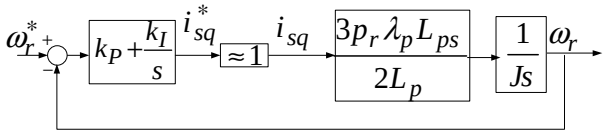

Fig. 6. Speed control loop of the secondary-side converter

The closed-loop transfer function for the speed control loop presented in Fig. 6 is:

$$\frac{\omega_r}{\omega_r^*} = \frac{k_p ms + k_i m}{s^2 + k_p ms + k_i m} \quad (20)$$

where $m = 3p_r L_{ps}\lambda_p / (2L_p J)$. Assuming $k_P << k_I$, (20) can be approximated as a second-order transfer function, and the *PI* controller gains can be calculated as follows:

$$\frac{\omega_r}{\omega_r^*} = \frac{k_i m}{s^2 + k_p ms + k_i m} = \frac{\omega_n^2}{s^2 + 2\xi\omega_n s + \omega_n^2} \quad (21)$$

$$k_P = \frac{2\xi\omega_n}{m} \quad , \quad k_I = \frac{\omega_n^2}{m} \quad (22)$$

V. Vector Control of Grid Side Converter (GSC)

The GSC is connected to the grid via a filter, as shown in Fig. 7. The major objective is to maintain the DC-link voltage at a given value and to regulate the active and reactive power exchange with the grid. The GSC is usually operated at unity power factor, but it can be used for voltage support during the grid fault by injecting reactive power into the grid [22]. Similar to the machine side power converter, the control part of the GSC includes two inner and one external control loop. This control is performed based on suitable relations that are explained in the following sections.

A. Mathematical model of the current loops

The voltage balance across the grid filter in the synchronous *dq* reference frame rotating at ω_p is given by:

$$\begin{cases} v_{gd} - v_{fd} = (R_f + L_f)i_{gd} - \omega_p L_f i_{gq} \\ v_{gq} - v_{fq} = (R_f + L_f)i_{gq} + \omega_p L_f i_{gd} \end{cases} \quad (23)$$

where R_f is the grid side filter resistance, L_f is its inductance, v_{gd} is the *d*-axis grid voltage, v_{gq} is the *q*-axis grid voltage, v_{fd} is the *d*-axis filter voltage, v_{fq} is the *q*-axis filter voltage, i_{gd} is the *d*-axis filter current, and i_{gq} is the *q*-axis filter current.

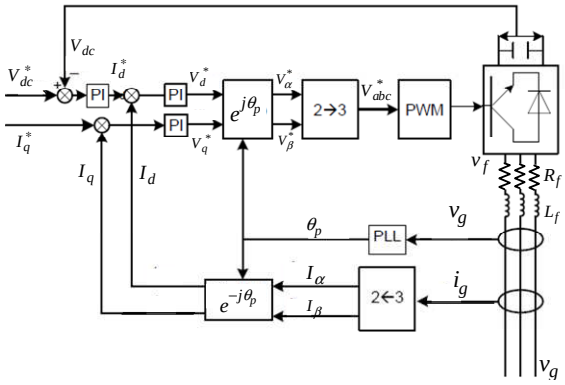

Fig. 7. Conventional vector control Grid Side converter

The grid-side converter current control loop shown in Fig. 8 has the following transfer function [23]:

$$\frac{i_{g_{dq}}}{i_{g_{dq}}^*} = \frac{\frac{k_P}{L_f}s + \frac{k_I}{L_f}}{s^2 + (\frac{R_f + k_P}{L_f})s + \frac{k_I}{L_f}} \approx \frac{\omega_n^2}{s^2 + 2\xi.\omega_n s + \omega_n^2} \quad (24)$$

$$k_P = (2\xi\omega_n L_f - R_f) \quad , \quad k_I = \omega_n^2 L_f \quad (25)$$

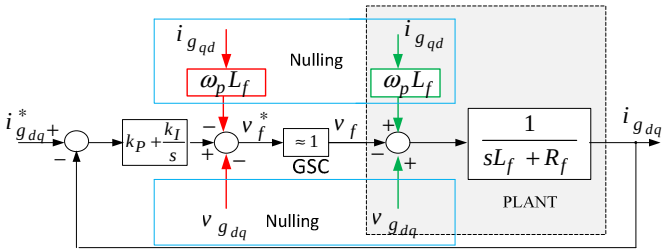

Fig. 8. Current control loops of the grid-side converter

VI. Simulation Results

A. Motoring operation

The results in Figs. 9-12 are obtained by running the VOC algorithm presented in Fig. 3 using *Matlab/Simulink*. The reference speed trajectory is set as a steep ramp signal suited for dynamically not very demanding wind power applications, even under extreme turbulent wind conditions. The MTPIA strategy has been implemented in Fig. 3 by setting the *Q** value for i_{sd} = 0 and $\lambda_p \approx v_p/\omega_p$. Fig. 9 shows an excellent speed tracking with no overshoot of the test BDFRG operating at synchronous (750 rev/min), super-synchronous (900 rev/min) and sub-synchronous (600 rev/min) speeds in the secondary frequency range of ±10Hz. The primary reactive power (*Q*) has been directly controlled at ≈1.35 MVAr obtained from (14) to minimize the i_{sd} magnitude for a given shaft torque and therefore to achieve the desired MTPIA performance.

For the case study under consideration, the simulated BDFRM has been assumed to have a shaft torque-speed profile as in [24] (where n_{rm} is the shaft speed, n_r is the rated speed of the machine, T_r is the rated torque of the machine and T_L is the load/turbine torque):

$$T_L = \pm T_r (\frac{n_{rm}}{n_r})^2 \quad (26)$$

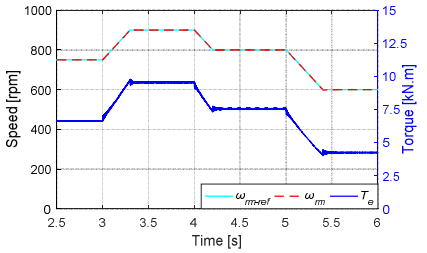

Fig. 9. BDFRG speed tracking and torque response.

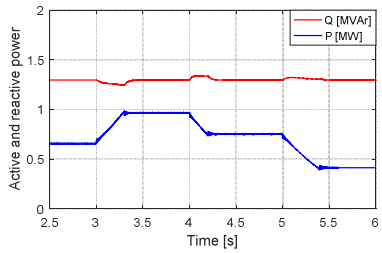

Fig. 10. Decoupled active and reactive power control.

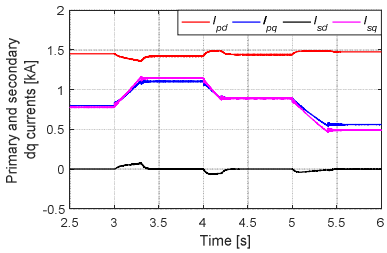

Fig. 11. MTPIA Primary and secondary *dq* currents.

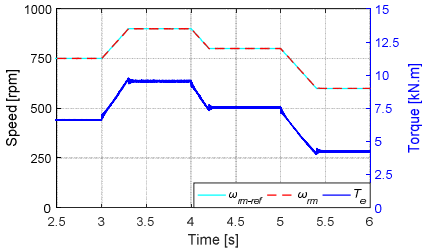

Fig. 12. BDFRM speed and torque for Q*=0.

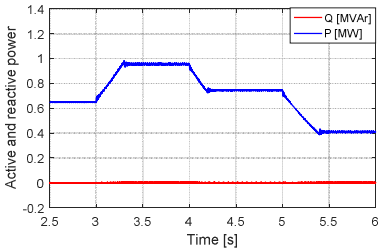

Fig. 13. Decoupled active and reactive power control for Q*=0.

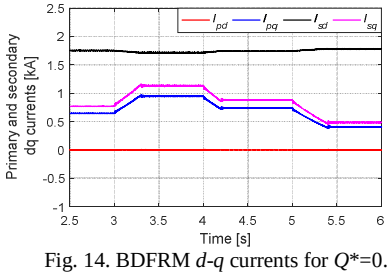

Fig. 14. BDFRM *d-q* currents for Q*=0.

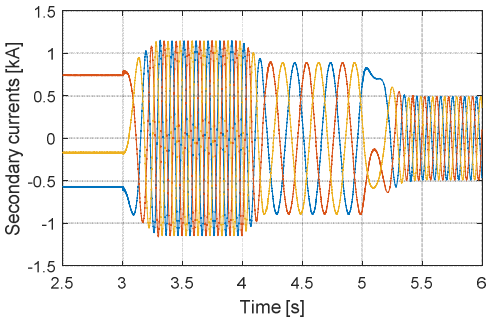

Fig. 15 Three phase secondary current waveform for the MTPIA strategy.

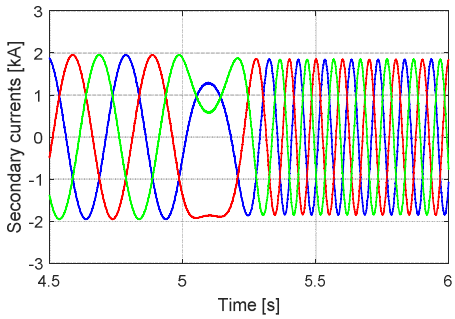

Fig. 16. The super to sub-synchronous speed mode transient at Q*=0.

The Q reference is often set to zero ($Q^* = 0$) for the unity primary power factor. The advantages of the first option (i.e. Q control disabled, speed control enabled, Fig. 3) are: one less *PI* controller to be tuned and completely independent control from the machine parameters. The second choice is model based, and thus less robust. The simulation results for the motoring operation at half-rated load of 9.5 kNm are presented in Figs. 12-14. The current i_{sd} ≈1800 A in Fig. 14 and i_{pd} = 0, what is complimentary to the Q = 0 as defined in (14). A three phase secondary current waveform for the MTPIA strategy is presented in Fig. 15, while Fig. 16 illustrates the transient stability of the machine while changing the machine speed from super-synchronous to sub-synchronous for Q*=0.

B. Generating operation

The simulation results for the machine operated as a generator are shown in Figs. 17-19. The remaining sub-plots show an excellent tracking of 750 rev/min, 900 rev/min, 800 rev/min and 600 rev/min set points (e.g. from 2.5s onward, after reaching the synchronous speed). The primary reactive power (Q) has been controlled at ≈ 1.35 MVAr, obtained from (14) for i_{sd} = 0 and $\lambda_p \approx v_p/\omega_p$ and the machine parameters are given in the Appendix. The secondary current components ($i_{s\_d,q}$) and their primary winding equivalents (i_{p_dq}) under the MTPIA conditions are presented in Fig. 19. The current i_{sd} ≈ 0, as expected for the minimum secondary current loading, while the i_{pd} is required to establish the machine flux and to satisfy the specific Q_p demand according to (14). The simulation results for Q = 0 are presented in Figs. 20-22.

VII. CONCLUSIONS

The paper presents a thorough simulation study and performance analysis of the VOC scheme developed for the optimum operation of the BDFRM, a viable DFIM competitor. The whole model is implemented in MATLAB/Simulink, in which the PI controllers are optimally designed. The simulation studies have evaluated the control algorithms using the parameters of a custom-designed 2 MW BDFRM in both motoring and generating modes, considering two control strategies. The first one has aimed at achieving the MTPIA by setting the command d-axis secondary winding current to zero in order to minimize the converter current loading, whereas the second one has targeted at the unity power-factor operation of the machine primary-winding by adjusting the command reactive power to zero. The simulation results presented have proven that the design methodology for the applied *PI* controllers can provide good performance and smooth response of the BDFRM.

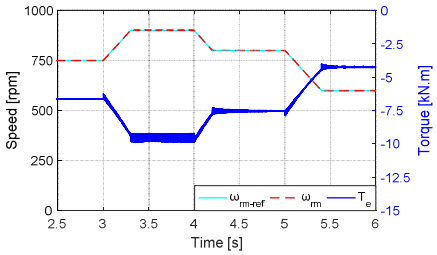

Fig. 17. BDFRM speed and torque for MTPIA (i_{sd}=0)

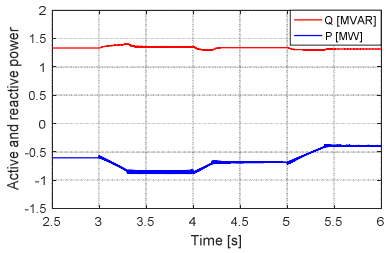

Fig. 18. BDFRG active, reactive power for MTPIA (i_{sd}=0).

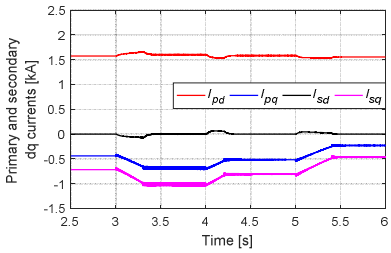

Fig. 19. BDFRG dq currents for MTPIA (i_{sd}=0).

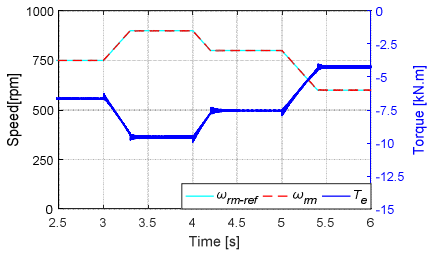

Fig. 20. BDFRM speed and torque for Q*=0.

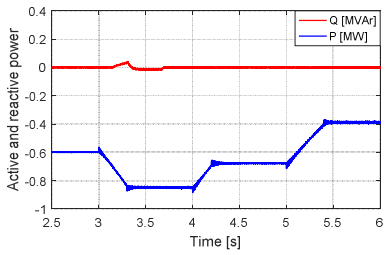

Fig. 21. BDFRG active, reactive power for Q*=0

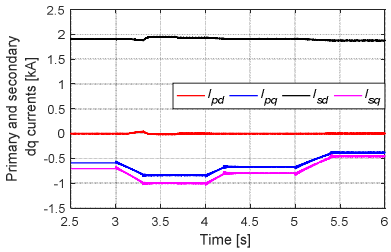

Fig. 22. BDFRG *dq* currents for Q*=0 (Fig. 21).

APPENDIX

TABLE **I:** THE BDFRM DESIGN SPECIFICATIONS

Rotor inertia [J]	3.8 kgm2	Rotor poles [p_r]	4
Primary resistance [Rp]	0.0375Ω	Primary power [P_r]	2 MW
Secondary resistance [R_s]	0.0575Ω	Rated speed [n_r]	900 rpm
Primary inductance [L_p]	1.17 mH	Stator currents [$I_{p,s}$]	1.5 kA rms
Secondary inductance [L_s]	2.89 mH	Primary voltage [V_p]	690 V rms
Mutual inductance [L_{ps}]	0.98 mH	Supply frequency [f_p]	50 Hz

ACKNOWLEDGMENT

This paper is a result within the project TR33017 which is supported by Ministry of Education, Science and Technological Development of the Republic of Serbia.

REFERENCES

[1] J. Carroll, A. McDonald and D. McMillan, "Reliability comparison of wind turbines with DFIG and PMG drive trains," IEEE Trans. on Energy Conversion, vol. 30, no. 2, pp. 663-670, 2015.

[2] M. Jovanovic, R. E. Betz and J. Yu, "The use of doubly fed reluctance machines for large pumps and wind turbines," IEEE Trans. on Ind. Applications, vol. 38, no. 6, pp. 1508-1516, 2002.

[3] E. M. Schulz and R. E. Betz, "Use of Doubly Fed Reluctance Machines in Wind Power Generation," in 12th Int. Power Elec. and Motion Control Conference, Portoroz, Slovenia, 2006.

[4] F. Zhang, S. Yu, Y. Wang, S. Jin and M. G. Jovanovic, "Design and Performance Comparisons of Brushless Doubly Fed Generators With Different Rotor Structures," IEEE Trans. on Industrial Electronics vol. 66, no. 1, pp. 631-640, January 2019.

[5] S. Ademi and M. Jovanović, "Maximum torque per inverter ampere control of brushless doubly-fed reluctance generators for wind turbines,"2014 Int. Symp. SPEEDAM, IEEE, pp. 883-888, 2014.

[6] Ademi and M. G. Jovanović, "Vector Control Methods for Brushless Doubly Fed Reluctance Machines," IEEE Trans. on Industrial Electronics, vol. 62, no. 1, pp. 96 - 104, Jan. 2015.

[7] F. Wang, F. Zhang and L. Xu, "Parameter and performance comparison of doubly-fed brushless machine with cage and reluctance rotors," IEEE Trans. on Ind. App, vol. 38, no. 5, p. 1237–1243, Sept./Oct. 2002.

[8] A. Ibrahim, M. I. Marei and H. S. El-Goharey, "Dynamic Responses Comparison of Control Techniques of BDFRG based WECS," International Journal of Scientific & Engineering Research, vol. 9, no. 11, pp. 1,672-1,678, November-2018.

[9] M. G. Jovanovic, R. E. Betzi, Y. Jian and E. Levi, "Aspects of Vector and Scalar Control of Brushless Doubly Fed Reluctance Machines," in 4th IEEE International Conference on Power Electronics and Drive Systems, vol. 2, pp. 461-467, 2001.

[10] M. Jovanovic, "Control of Brushless Doubly-Fed Reluctance Motors," in in ISIE 2005, Dubrovnik, Croatia, 2005.

[11] S. Ademi and M. Jovanovic, "Vector control strategies for brushless doubly-fed reluctance wind generators," in 2nd Int. Symp. EFEA, Newcastle upon Tyne, UK, 2012.

[12] L. Xu, L. Zhen and E.-H. Kim, "Field-orientation control of a doubly excited brushless reluctance machine," IEEE Trans. on Industry Applications, vol. 34, no. 1, pp. 148 - 155, Jan/Feb 1998.

[13] M. Jovanovic, "Sensored and sensorless speed control methods for brushless doubly fed reluctance motors," IET Electric Power Applications, vol. 3, no. 6, pp. 503 - 513, November 2009.

[14] M. Jovanovic, J. Yu and E. Levi, "Encoderless direct torque controller for limited speed range applications of brushless doubly fed reluctance motors," IEEE Transactions on Industry Applications, vol. 42, no. 3, pp. 712 - 722, May-June 2006.

[15] H. Chaal and M. Jovanovic, "Practical Implementation of Sensorless Torque and Reactive Power Control of Doubly Fed Machines," IEEE Trans. on Ind. Electronics, vol. 59, no. 6, pp. 2645 - 2653, June 2012.

[16] H. Chaal and M. Jovanovic, "Toward a Generic Torque and Reactive Power Controller for Doubly Fed Machines," IEEE Trans.on Pow. Electronics, vol. 27, no. 1, pp. 113 - 121, Jan. 2012.

[17] H. Chaal and M. Jovanovic, "Power control of brushless doubly-fed reluctance drive and generator systems," Renewable Energy, vol. 37, no. 1, pp. 419-425, January 2012.

[18] M. Moazen, R. Kazemzadeh and M.-R. Azizian, "Model-based predictive direct power control of brushless doubly fed reluctance generator for wind power applications," Alexandria Engineering Journal, vol. 55, no. 3, pp. 2497-2507, September 2016.

[19] R. E. Betz and M. G. Jovanovic, "Introduction to the Space Vector Modeling of the Brushless Doubly Fed Reluctance Machine," in Electric Power Components and Systems, Taylor & Francis Inc., 2003, pp. 729–755.

[20] T. Lei, Doubly-fed induction generator wind turbine modeling, control and reliability, Manchester, UK: [Thesis]. The University of Manchester, 2014.

[21] H. Abu-Rub, M. Malinowski and K. Al-Haddad, Power Electronics for Renewable Energy Systems, Transportation and Industrial Applications, John Wiley & Sons, 2014.

[22] L. V. Dai and D. D. Tung, "Modeling for Development of Simulation Tool: A Case Study of Grid Connected Doubly Fed Induction Generator Based on Wind Energy Conversion System," International Journal of Applied Engineering Research ISSN 0973-4562, vol. Volume 12, pp. pp. 2981-2996, 2017.

[23] M. Zarif, M. Monfared, " Step-by-step design and tuning of VOC control loops for grid connected rectifiers," International Journal of Electrical Power & Energy Systems, vol.64, pp. 708–713, 2015

[24] S. Ademi, M. Jovanovic and J. K. Obichere, "Comparative Analysis of Control Strategies for Large Doubly-Fed Reluctance Wind Generators," in Proc. of the World Congress on Engineering and Computer Science, San Francisco, USA, October, 2014.